PROJECT FINAL REPORT for Korean – AFOSR Nanoscience and Technology Initiative
<AOARD-054084>

< Fabrications and Characterizations of $ZnO/Zn_{1-x}Mg_xO$ Nanorod Quantum Structures >

< November 8, 2005>

Name of Principal Investigator: Prof. Gyu-Chul Yi

Institution: Pohang University of Science and Technology (POSTECH)
Mailing address: National CRI Center for Semiconductor Nanorods
Dept. of Materials Science and Engineering
POSTECH
San-31 Hyoja-dong
Pohang, Kyungbuk 790-784
Korea (ROK)
Phone: +82-54-279-2155
FAX: +82-54-279-8635
e-mail address: gcyi@postech.ac.kr

Report Documentation Page

Form Approved
OMB No. 0704-0188

1. REPORT DATE	2. REPORT TYPE	3. DATES COVERED
23 OCT 2007	**FInal**	**12-05-2005 to 11-11-2005**

4. TITLE AND SUBTITLE
Fabrications and Photoluminescent Characterizations of ZnO/Zn1-xMgxO Nanorod Quantum Structures

5a. CONTRACT NUMBER
FA520905P0462

5b. GRANT NUMBER

5c. PROGRAM ELEMENT NUMBER

6. AUTHOR(S)
Gyu Chul Yi

5d. PROJECT NUMBER

5e. TASK NUMBER

5f. WORK UNIT NUMBER

7. PERFORMING ORGANIZATION NAME(S) AND ADDRESS(ES)
Pohang Univ. of Science & Technology,San-31 Hyoja-dong,Pohang, Kyungbuk 790-784,Korea (South),KR,790-784

8. PERFORMING ORGANIZATION REPORT NUMBER
N/A

9. SPONSORING/MONITORING AGENCY NAME(S) AND ADDRESS(ES)
AOARD, UNIT 45002, APO, AP, 96337-5002

10. SPONSOR/MONITOR'S ACRONYM(S)
AOARD

11. SPONSOR/MONITOR'S REPORT NUMBER(S)
AOARD-054084

12. DISTRIBUTION/AVAILABILITY STATEMENT
Approved for public release; distribution unlimited

13. SUPPLEMENTARY NOTES

14. ABSTRACT
This project investigated photoluminescent properties of ZnO/ZnMgO coaxial nanorod heterostructures and ZnO/ZnMgO nanorod single-quantum-well structures (SQWs). Individual nanorod SQWs were characterized by scanning near-field optical microscopy.

15. SUBJECT TERMS
Nanotechnology, Zinc Oxide

16. SECURITY CLASSIFICATION OF:			17. LIMITATION OF ABSTRACT	18. NUMBER OF PAGES	19a. NAME OF RESPONSIBLE PERSON
a. REPORT	b. ABSTRACT	c. THIS PAGE			
unclassified	**unclassified**	**unclassified**	**Same as Report (SAR)**	**11**	

Overview

Among many one-dimensional (1D) nanorod heterostructures composition modulated along the radial directions nanorod heterostructures have been fashioned into versatile building blocks for many electronic and photonic nanodevice applications. For instance, if a shell layer in a coaxial nanorod heterostructure has a wider bandgap energy and a lower refractive index than a core layer, confinement of both carriers and photons in the core nanorod is significantly enhanced, which enables fabrication of highly efficient light emitting devices as already proven for quantum well or quantum wire semiconductor lasers. In addition, low-dimensional carrier gas is formed for coaxial nanorod hetrerostructures with abrupt interfaces, essential for fabrication of nanometer-scale transistors with high carrier mobility. Nevertheless, a rational synthetic strategy for 1D heterostructures, which can fulfill various application requirements, is not yet fully established. In this research, we investigated photoluminescent (PL) properties of ZnO/ZnMgO coaxial nanorod heterostructures and ZnO/ZnMgO nanorod single-quantum-well structures (SQWs). Especially, scanning near-field optical microscopy (SNOM) has been used for optical characterizations of individual nanorod SQWs.

Introduction

Among many one-dimensional (1D) nanorod heterostructures composition modulated along the radial directions nanorod heterostructures have been fashioned into versatile building blocks for many electronic and photonic nanodevice applications. For instance, if a shell layer in a coaxial nanorod heterostructure has a wider bandgap energy and a lower refractive index than a core layer, confinement of both carriers and photons in the core nanorod is significantly enhanced, which enables fabrication of highly efficient light emitting devices as already proven for quantum well or quantum wire semiconductor lasers. In addition, low-dimensional carrier gas is formed for coaxial nanorod hetrerostructures with abrupt interfaces, essential for fabrication of nanometer-scale transistors with high carrier mobility. Nevertheless, a rational synthetic strategy for 1D heterostructures, which can fulfill various application requirements, is not yet fully established. Although 1D coaxial nanowire heterostructures including GaN/(Al,Ga)N and ZnO/(Mg,Zn)O have recently been fabricated by the vapor-liquid-solid (VLS) process, a clean and abrupt interface has not been produced, presumably due to spontaneous phase separation inducing self-ordered formation of coaxial heterostructures. In particular, difficulties with thickness and composition controls of the each layer hinder us from synthesizing artificial heterojunction structures. These exciting challenges in overcoming such problems inspire us to facilitate sophisticated metal-organic vapor phase epitaxy (MOVPE) for attaining accurate layer thickness and composition controls of coaxial nanorod heterostructures.

Coaxial nanowire/nanorod heterostructures with composition modulation along the radial direction can be used as an essential component for fabrication of quantum devices, such as high electron mobility transistors. For ZnO/ZnMgO core-shell nanorod heterostructures, the higher bandgap energy and larger refractive index of the ZnMgO shell layer result in confining both the carriers and emitted photons. In addition, the shell layer coating on ZnO core nanorods with a clean interface is expected to suppress surface-mediated nonradiative recombination and to decrease thermal quenching of light emission intensity. Although there have been some reports on coaxial nanowire and nanorod heterostructures, including Ge/Si, Si/CdSe, and GaP/GaN, the enhanced optical properties of coaxsial nanorod heterostructures have not been reported. However, since the lattice mismatches between ZnO and $Zn_{0.8}Mg_{0.2}O$ are smaller than 1 %, we can prepare high quality $ZnO/Zn_{0.8}Mg_{0.2}O$ coaxial nanorod heterostructures with clean interfaces, enabling us to successfully demonstrate the quantum confinement effect in the nanorod quantum structures.

Recent demonstration of semiconductor nanorod quantum-well structure enables us to fabricate nanometer-scale electronic and photonic devices on single nanorods. Recently, several ZnO/ZnMgO nanorod quantum structures were fabricated and the quantum confinement effect was successfully observed. In addition, further improvement in the fabrication of nanorod heterostructures has resulted in the observation of significant PL intensity, even from ZnO/ZnMgO nanorod single-quantum-well structures (SQWs). Near-field spectroscopy has made a remarkable contribution to investigations of the optical properties in nanostructures, and resulted in the observation of nanometer-scale optical image, such as the local density of exciton states. To confirm the promising optical properties of individual ZnO/ZnMgO SQWs for realizing nanophotonic devices, we investigated optical anisotropy and spatially-resolved PL emission of ZnO/ZnMgO SQWs using near-field spectroscopy.

Results

1. Fabrication and photoluminescent properties of heteroepitaxial ZnO/$Zn_{0.8}Mg_{0.2}O$ coaxial nanorod heterostructures

$ZnO/Zn_{1-x}Mg_xO$ coaxial nanorod heterostructures were synthesized by *in-situ* heteroepitaxial growth of a $Zn_{1-x}Mg_xO$ thin layer on ZnO core nanorods. MOVPE was employed for the fabrication of $Zn_{1-x}Mg_xO/ZnO$ coaxial nanorods with an abrupt interface, homogeneous compositions, and a uniform layer thickness.[11] We employed a two-step MOCVD process consisting of (i) high temperature synthesis of ultrafine core ZnO nanorods and (ii) subsequent low temperature $Zn_{1-x}Mg_xO$ shell layers coated on core ZnO to fabricate the $ZnO/Zn_{1-x}Mg_xO$ coaxial nanorod heterostructures, as schematically shown in Fig. 1(a). As an initial step, core ultrafine ZnO nanorods were prepared at 800–900°C using diethylzinc (DEZn) and oxygen as the reactants, with argon as the carrier gas. Nanorod diameters determined by electron microscopy images were as small as 9 nm with a normalized standard deviation value (a standard deviation divided by a mean) of 0.2–0.3. Subsequent depositions of $Zn_{1-x}Mg_xO$ shell layers were *in-situ* performed at low temperature of 450–550°C by addition of *bis*-cyclopentadienyl-Mg (cp_2Mg) as the Mg precursor in the same chamber, resulting in a $Zn_{1-x}Mg_xO$ layer coating over all ZnO nanorod surfaces. The $Zn_{1-x}Mg_xO$ shell layer coating on the ultrafine ZnO nanorods was robust and was not peeled off.

Figure 1(b) shows a typical field-emission scanning electron microscopy (FE-SEM) image of $ZnO/Zn_{0.8}Mg_{0.2}O$ coaxial nanorod heterostructures. In comparison with bare ZnO nanorods, there is no significant change in the morphology except that nanorod diameters increased with $Zn_{0.8}Mg_{0.2}O$ shell coating time. As shown in Figs. 1(c) and (d), furthermore, HR-TEM images were obtained by TEM measurements of the nanorod heterostructures along longitudinal and transverse (cross-sectional) directions of the nanorods, which clearly revealed the formation of $ZnO/Zn_{0.8}Mg_{0.2}O$ coaxial nanorod heterostructures by the contrast change due to the composition difference between core and shell layers along the radial direction. For the transverse directional TEM measurements, the coaxial nanorod heterostructures were sliced, perpendicular to the c-axis of the nanorods using an ultramicrotome. The cross-sectional TEM image of the $ZnO/Zn_{0.8}Mg_{0.2}O$ coaxial nanorod heterostructure exhibits well-developed {10-10} facets in the ZnO core with an abrupt interface between ZnO and $Zn_{0.8}Mg_{0.2}O$. These TEM images indicate that the $Zn_{0.8}Mg_{0.2}O$ shell layers with a thickness of 11–14 nm covered the entire surfaces of the ZnO core nanorod continuously and uniformly. Based on the shell layer thickness measurements by both TEM and SEM, the coating rate was estimated to be 3.2 nm/min.

The HR-TEM image also shows very clean and abrupt interfaces between the ZnO and $Zn_{0.8}Mg_{0.2}O$ layers as indicated by arrows in the TEM images. Apart from the difference in TEM image contrast, the lattice images of both layers were hardly distinguishable and the interface was not easily recognizable as shown in Fig. 1(e). Dislocations at the interfaces or at the shell layer were rarely observed, as little as at the bare ZnO layer, while dislocations were quite often observed for lattice-mismatched GaN/ZnO coaxial nanorod heterostructures. The electronic structure observed from the electron energy-loss spectrometer also showed little difference in the conduction band structure of oxygen K-edge at ZnO and $Zn_{0.8}Mg_{0.2}O$ layers. These TEM results

strongly suggest that the growth of $Zn_{0.8}Mg_{0.2}O$ on ZnO is coherently epitaxial, presumably resulting from the small lattice mismatch between ZnO and $Zn_{0.8}Mg_{0.2}O$ layers less than 0.5 %.

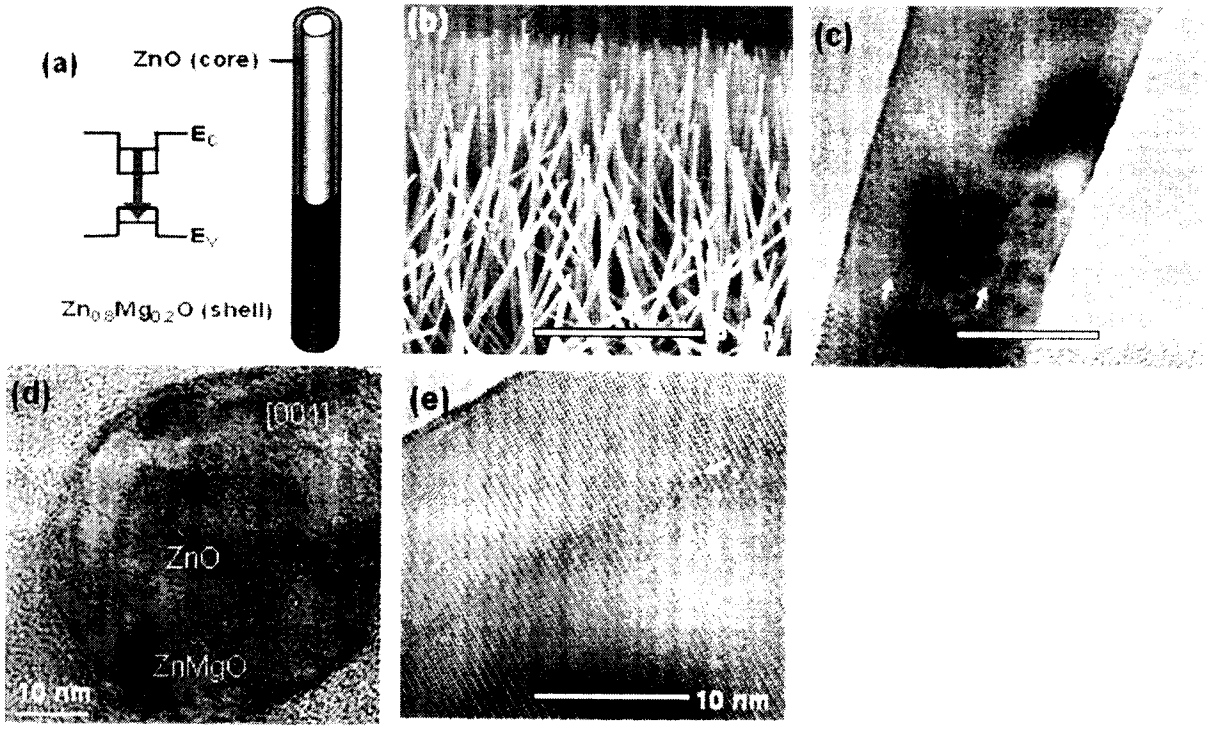

Figure 1. (a) Schematic and (b-e) electron microscopy images of $ZnO/Zn_{0.8}Mg_{0.2}O$ coaxial nanorod heterostructures. (b) Typical FE-SEM images of $ZnO/Zn_{0.8}Mg_{0.2}O$ coaxial nanorod heterostructures. TEM images of $ZnO/Zn_{0.8}Mg_{0.2}O$ coaxial nanorod heterostructures measured along (c) longitudinal and (d) transverse (cross-sectional) directions. The cross-sectional TEM image of the $ZnO/Zn_{0.8}Mg_{0.2}O$ coaxial nanorod heterostructure exhibit well-developed {10-10} facets in the ZnO core with an abrupt interface between ZnO and $Zn_{0.8}Mg_{0.2}O$. (e) HR-TEM image of $ZnO/Zn_{0.8}Mg_{0.2}O$ coaxial nanorod heterostructures. From the HR-TEM measurements, lattice images of the nanorod heterostructures without any visible defect formation were clearly observed.

Figures 2(a)-(d) show room temperature PL spectra of ZnO nanorods with average diameters of 9 and 35 nm, and $ZnO/Zn_{0.8}Mg_{0.2}O$ coaxial nanorod heterostructures. As shown in Figures 3(a) and (b), the dominant PL peak of ultrafine ZnO core nanorods with a diameter of 9 nm shows a 30-meV blue-shift, compared with that of thick ZnO nanorods with a diameter of 35 nm due to the quantum confinement effect. In addition, overall shape and dominant peak positions in the spectra from the thin ZnO nanorods are not significantly affected by the $Zn_{0.8}Mg_{0.2}O$ shell layer coating. In particular, the PL peak position of $ZnO/Zn_{0.8}Mg_{0.2}O$ coaxial nanorod heterostructures did not significantly depend on the thickness of the capping $Zn_{0.8}Mg_{0.2}O$ layer. However, for only the heterostructures with a $Zn_{0.8}Mg_{0.2}O$ shell layer thicker than 20 nm, a new emission peak was observed at 3.53 eV, corresponding to the near bandedge emission of the $Zn_{0.8}Mg_{0.2}O$ layer. From all the above results, the possibility of alloy formation and resulting blue-shift of the PL peak can be ruled out, indicating that there is no significant intermediate layer formation in MOVPE growth of the coaxial nanorod heterostructures.

One of significantly enhanced PL properties for coaxial nanorod heterostructures is much higher PL intensity than that of bare ZnO nanorods. As shown in the inset of Fig. 2(a), the integrated PL intensity of nanorod heterostructures increased with the $Zn_{0.8}Mg_{0.2}O$ layer thickness coating. This behavior is presumably related to surface state effects on radiative recombination of the coaxial nanorod heterostructures. In general, the surface acts like a defect and may induce nonradiative or radiative deep level transitions. This surface effect is more serious for the thinner nanorods due to their higher surface/volume ratio. For the coaxial nanorod heterostructure, the $Zn_{0.8}Mg_{0.2}O$ shell layer can confine carriers in the ZnO core, and hence suppress luminescent quenching by the surface state effect. In addition, the enhancement of the integrated PL intensity became higher with increasing $Zn_{0.8}Mg_{0.2}O$ layer thickness up to 13 nm, presumably due to the increased excitation volume for thicker nanorod heterostructures. However, further increases of shell layer thickness over 13 nm leads to a small decrease in the PL intensity This may result from another radiative transition at 3.53 eV in $Zn_{0.8}Mg_{0.2}O$ or nonradiative transition by misfit dislocations. Dislocation density may start to increase significantly, as the shell layer thickness exceeds a certain critical thickness, thereby increasing the probability of carrier trapping to nonradiative recombination centers.

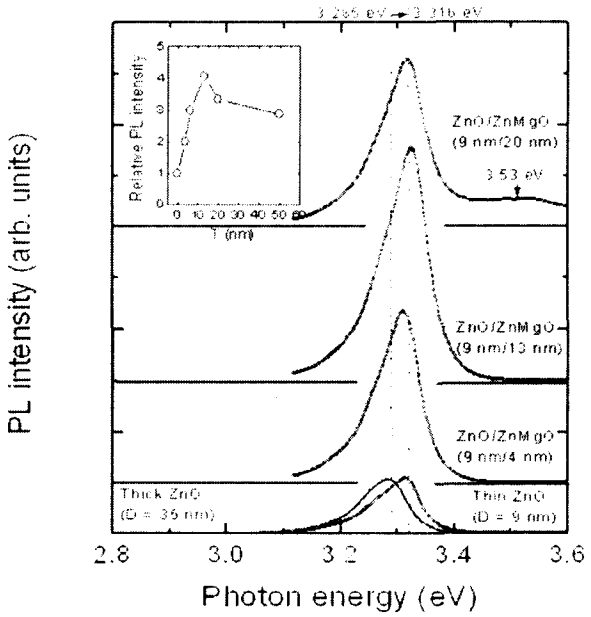

Figure 2. Room temperature PL spectra of ZnO nanorods with average diameters of (a) 9 and (b) 35 nm, and (c) $ZnO/Zn_{0.8}Mg_{0.2}O$ coaxial nanorod heterostructures. The inset shows the normalized PL intensity of near bandedge emissions, depending on the $Zn_{0.8}Mg_{0.2}O$ shell layer thickness.

Further optical properties of $ZnO/Zn_{0.8}Mg_{0.2}O$ coaxial nanorod heterostructures were investigated by measuring their PL spectra at various temperatures between 10 K and room temperature. Figure 3(a) shows typical temperature-dependent PL spectra of ZnO (9 nm diameter)/$Zn_{0.8}Mg_{0.2}O$ (13 nm thickness) coaxial nanorod heterostructures. With increasing temperature, thermal quenching in the dominant PL peak was observed with a red shift of the dominant PL peak due to band gap shrinkage. For the coaxial nanorod heterostructures, however, thermal quenching is much lower than that of bare ZnO nanorods. From temperature-dependent integrated emission intensity for thick and ultrafine ZnO nanorods and the $ZnO/Zn_{0.8}Mg_{0.2}O$

coaxial nanorod heterostructures as shown in Fig. 3(b), the coaxial nanorod heterostructures exhibited the lowest thermal quenching. This results from reduced thermal escape to nonradiative centers since radiative transition by electron and hole wavefunction overlap is enhanced due to carrier localization in the ultrafine ZnO nanorods and their coaxial heterostructures. Furthermore the high quality heteroepitaxial $Zn_{0.8}Mg_{0.2}O$ capping layer passivates surface nonradiative recombination centers, resulting in the reduced thermal quenching.

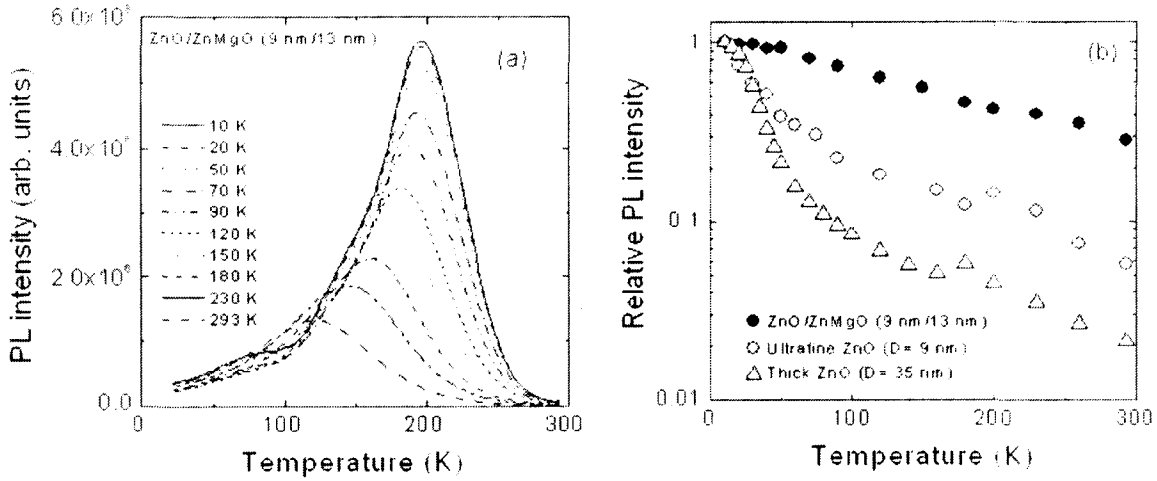

Figure 3. Temperature-dependent PL spectra of ZnO (9 nm diameter)/$Zn_{0.8}Mg_{0.2}O$ (13 nm thickness) nanorod heterostructures measured in the temperature range from 10 to 293 K. (b) Spectrally-integrated PL intensity normalized with the PL intensity at 10 K as a function of temperature for thick (D = 35 nm) and ultrafine (D = 9 nm) ZnO nanorods and ZnO/$Zn_{0.8}Mg_{0.2}O$ coaxial nanorod heterostructures.

Our controlled heteroepitaxial growth of coaxial nanorod heterostructures opens up significant opportunities for fabrication of nanorod device structures with radial composition modulation. In particular, these coaxial nanorod heterostructures may be very useful for high efficiency light-emitting device applications.

2. Evaluating quantum confinement effect of isolated ZnO nanorod single-quantum-well structures using near-field measurement

ZnO/ZnMgO SQWs were fabricated on the ends of ZnO nanorods with a mean diameter of 40 nm using catalyst-free metalorganic vapor phase epitaxy. The average concentration of Mg in the ZnMgO layers used in this study was determined to be 20 at. %. The ZnO well layer thickness L_W investigated in this study were 2.5, 3.75, and 5.0 nm, while the thickness of the ZnMgO bottom and top barrier layers in the SQWs were fixed at 60 and 18 nm, respectively. After the growth of ZnO nanorod SQWs on sapphire (0001) substrate, they were dispersed on the substrate to be isolated. To confirm the promising optical properties of individual ZnO SQWs, we used collection-mode NOM at 15K, in which He-Cd laser (λ=325 nm) was used for the excitation. We used UV fiber probe with an aperture diameter of 30 nm [Fig. 4].

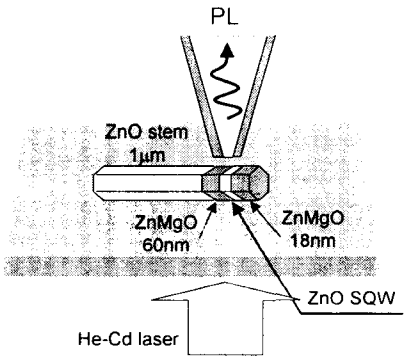

Fig. 4. Schematic of near-field spectroscopy of the isolated ZnO SQWs on the ends of ZnO nanorod.

A major investigation of the optical properties of isolated ZnO SQWs was performed by analyzing the polarization-dependent PL spectrum of isolated ZnO SQWs (L_w = 3.75 nm). As shown in Fig. 5(a), NF_0 is a near-field PL spectrum obtained with parallel polarization with respect to the c-axis, $\theta = 0^\circ$, and this exhibits a new peak I_{1b}^{QW} at 3.483 eV, which is out of peak in the far-field spectrum (3.435 eV ± 20 meV). As the ZnO has valence band anisotropy owing to the wurtzite crystal structure, the operator corresponds to the Γ_5 (Γ_1) representation when the electric vector $\boldsymbol{E}$ of the incident light is perpendicular (parallel) to the crystalline c-axis, respectively. By considering the energy difference between Γ_5 and Γ_1 in the center of the zone around 40 meV for bulk material, and the direction of the incident light polarization with respect to the c-axis, emission peaks I_{1a}^{QW} and I_{1b}^{QW} in Fig. 5(a) are allowed for the exciton from Γ_5 and Γ_1, respectively. This successful observation of a Γ_1 exciton in a PL spectrum originates from the enhancement of the exciton binding energy owing to the quantum confinement effect because the exciton binding energy of the emission from Γ_1 (50-56 meV) is comparable to that from Γ_5 (60 meV). The homogeneous linewidth of emission peak I_{1a}^{QW} (Γ_5) is in the range 3-5 meV, while that of I_{1b}^{QW} (Γ_1) is 9-11 meV [Fig. 5(b)]. This difference is attributed to the degeneracy of the transition of the Γ_1 exciton with continuum and to the contribution of the residual strain field, and results in sensitive dependence of the Γ_1 exciton on the strain. The solid triangles and circles in Fig. 5(c) shows the respective normalized integrated PL intensity at I_{1a}^{QW} and I_{1b}^{QW}, respectively, which are in good agreement with the sine-squared and cosine-squared functions represented by the solid curves. These results indicate that emission peaks I_{1a}^{QW} and I_{1b}^{QW} originate from unidirectional transition dipoles that are orthogonal each other.

To study the linewidth broadening mechanism, Fig. 5(d) shows the polarization-dependent near-field PL spectra (NF_0-NF_{90}) and absorption spectrum obtained for isolated ZnO SQWs with a thinner well layer (L_w = 2.5 nm). In NF_0-NF_{90}, the emission peaks I^{ZnMgO} around 3.535 eV originate from the ZnMgO layers. Emission peak I_{2a}^{QW} originates from the Γ_5 exciton in the SQWs, as was the case for I_{1a}^{QW} in Fig. 5(a), since the position of peak I_{2a}^{QW} (3.503 eV) is comparable to that of the dominant peak in the far-field PL spectra (3.480 eV) and the theoretical prediction (3.455 eV) using the finite square-well potential of the quantum confinement effect in the ZnO well layer. In comparison to ZnO SQWs with L_w = 3.75 nm, however, emission peak I_{2a}^{QW} had a broader linewidth (7-10 meV), which is attributed to the shorter exciton dephasing time. In the nanocrystallite where the excitons are quantized, the linewidth should be determined by the exciton dephasing time. Such dephasing arises from the collisions of the excitons at the

irregular surface, so that the linewidth is d^{-2} (d is the effective size of the quantum structure). The observed well-width dependence of the spectral linewidth, $3.75^{-2}/2.5^{-2}\sim3/7$, and the Stokes shift of 7 meV [see Fig. 5(c)] larger than that for L_w = 3.75 nm (3 meV) are supported by this dephasing mechanism quantitatively. Although emission peak I_{2a}^{QW} was suppressed for θ=0°, no peaks corresponding to the Γ_1 exciton in SQWs were detected owing to the reduction of the exciton binding energy, since the peak energy of Γ_1 for the ZnO SQWs with L_w = 2.5 nm is comparable with that of ZnMgO.

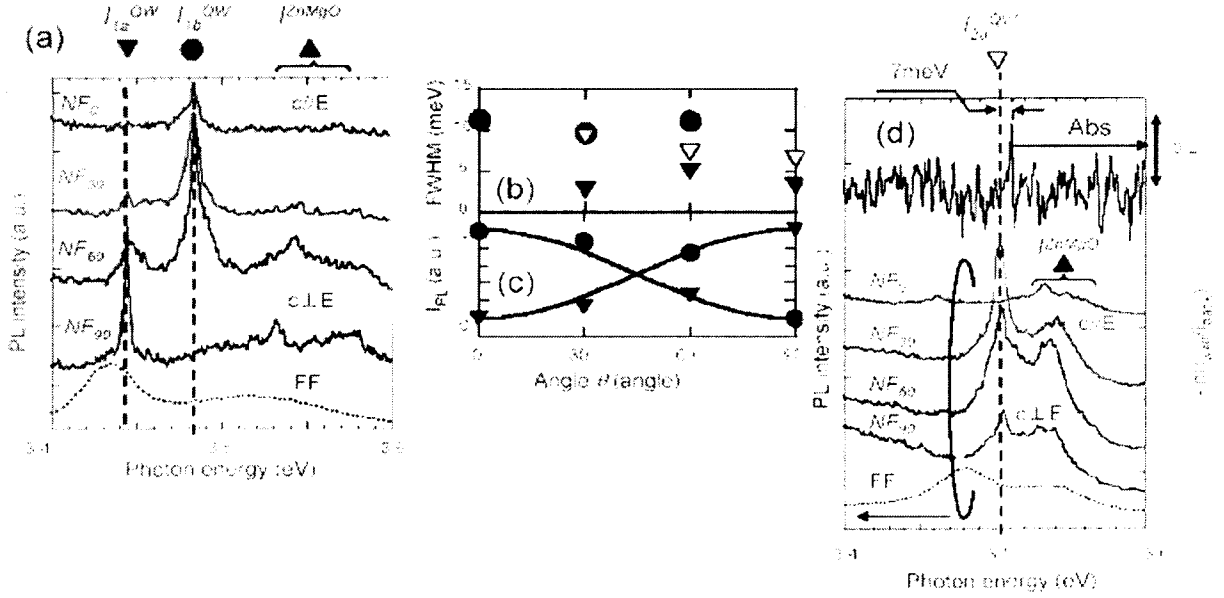

Fig. 5. Polarization-dependence of near-field PL spectra of isolated ZnO SQWs obtained at 15 K. (a) *NF* , *FF*: near-field and far-field PL spectra of isolated ZnO SQWs (L_w = 3.75 nm) for =0, 30, 60, and 90 degrees. (b) Solid triangles and circles are the polarization dependence of the linewidth of I_{1a}^{QW} and I_{1b}^{QW}, respectively in (a). Open triangles are the polarization dependence of linewidth of I_{2a}^{QW} in (d). (c) Solid triangles and circles are the integrated PL intensities, I_{PL}, of I_{1a}^{QW} and I_{1b}^{QW}, respectively, normalized to the total PL intensities ($I_{1a}^{QW} + I_{1b}^{QW}$). (d) *NF* , *FF*: near-field and far-field PL spectra of isolated ZnO SQWs (L_w = 2.5 nm). *Abs.*: absorption spectrum.

Near-field PL spectrum of the nanorod SQWs with L_w = 5.0 nm (NF_a) shows broader spectral width of I_a^{SQW} with an additional peak at 3.395 eV (I_a). In order to determine the origin of the I_a emission peak, we obtained spatially-resolved near-field PL spectra along the axial direction of ZnO SQWs of L_w = 5.0 nm (Fig. 6). Curves from 1 to 14 shown in Fig. 6(a) correspond to the near-field PL spectra obtained for every 18 nm from the left- to right-hand side along the dashed white line in Fig. 6(b). Curve 10 of *NF* and curve *FF* in Fig. 6(a) are the same as curves NF_a and FF_a in Fig. 5(a), respectively. Figs. 6(b)-6(f) show the spatially and spectrally resolved PL images at 3.365, 3.393, 3.400, 3.410, and 3.550 eV, respectively. Several conclusions can be drawn from these spatial distributions. First, the full width at half maximum of linear shaped distribution of I_2^{ZnO} at 3.365 eV [Fig. 6(b)] was as small as 20 nm. This result confirms that this distribution is originated from the isolated ZnO SQWs nanorod. Second, comparison between the cross-sectional profiles along the dashed white lines in Figs. 6(b) and 6(e) reveals that the peak intensity at 3.365 eV (I_2^{ZnO}) from the ZnO stem decrease, while the emission at 3.410 eV from the SQW (I_a^{SQW}) remained to the end of the nanorod (see also curves *B* and *E* in Fig. 6(g)). This result supports the postulate that the blue shifted emission at 3.410

eV (I_a^{SQW}) was confined to the end of the ZnO stem, surrounded by the ZnMgO barrier layers [see curve *F* in Fig. 6(g)]. Third, the emission peak of I_a divided into two peaks of 3.393 eV (I_{a1}: Fig. 6(c)) and 3.400 eV (I_{a2}: Fig. 6(d)), and that the peak intensity of I_{a1} decreases, while the peak intensity of I_{a2} increases at the end of the nanorod. From the corresponding cross-sectional profiles [curves *C* and *D* in Fig. 6(g)], we found that these peaks are located at interfaces of the ZnO well layer and top and bottom ZnMgO layer, respectively [indicated by the arrows F_1 and F_2 in Fig. 6(h)]. These results suggest that the two peaks are presumably originated from the well-width fluctuations or the strain induced at the ZnO/ZnMgO interface because the well-width is large as 5 nm [see Fig. 6(h)].

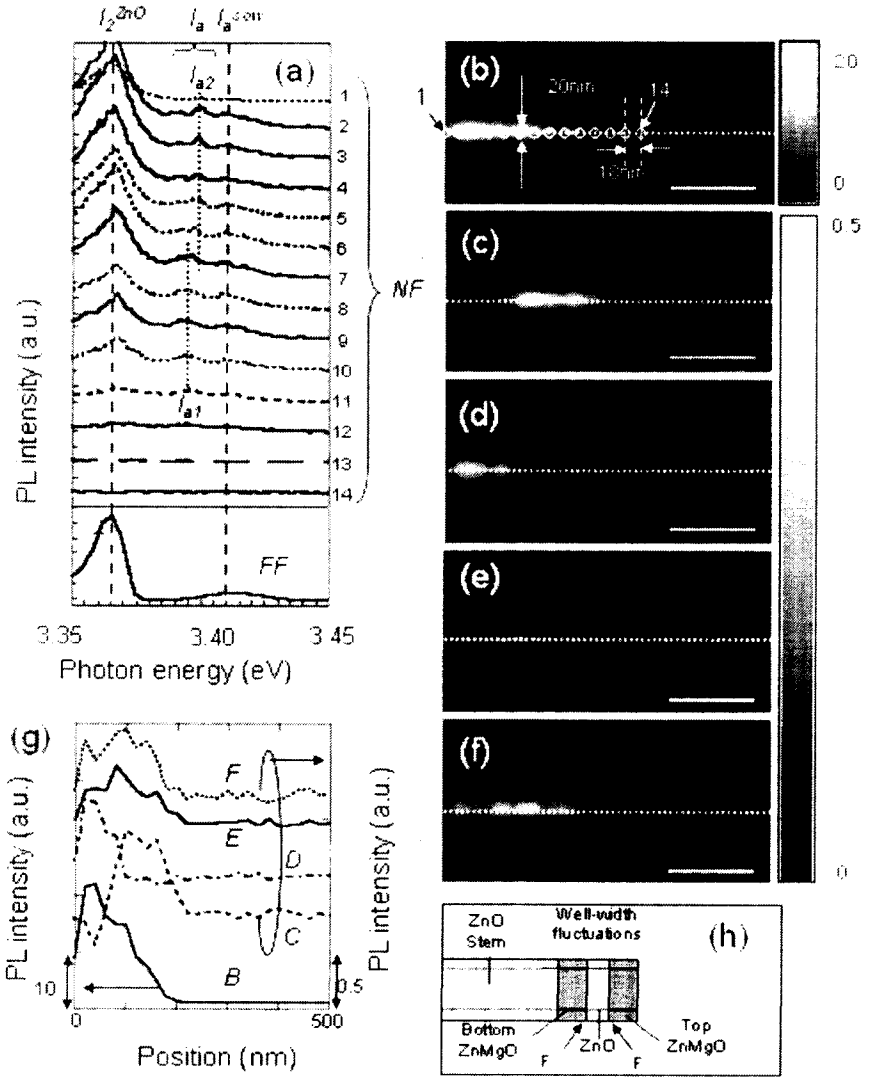

Fig. 6. (a) Low-temperature (15 K) far-field PL spectra of vertically aligned ZnO nanorod SQWs (*FF*) and near-field PL spectra (*NF*) of the isolated ZnO SQWs (L_W=5.0 nm). Spatial distributions at the peaks of (b) 3.365 (I_2^{ZnO}), (c) 3.393 (I_{a1}), (d) 3.400 (I_{a2}), (e) 3.410 (I_a^{SQW}), and (f) 3.550 eV (I^{ZnMgO}). Scale bars: 100 nm. (g) Curves B-F show the cross-sectional profiles along the dashed white line in (b)-(f). (h) Schematic of the ZnO nanorod SQWs. Arrows F_1 and F_2 indicate the interfaces between the ZnO well layer and ZnMgO layers.

The near-field PL measurement of isolated SQWs described above is a promising step toward designing a nanophotonic switch and related devices.

Achievements

1. Won Il Park, Jinkyoung Yoo, Dong Wook Kim, **Gyu-Chul Yi**, and Miyoung Kim. "Fabrication and photoluminescent properties of heteroepitaxial ZnO/$Zn_{0.8}Mg_{0.2}O$ coaxial nanorod heterostructures", Journal of Physical Chemistry B (submitted).

2. Takashi Yatsui, Motoich Ohtsu, Sung Jin An, Jinkyoung Yoo, and **Gyu-Chul Yi**, "Evaluating the quantum confinement effect of isolated ZnO nanorod single-quantum-well structures using near-field ultraviolet photoluminescence spectroscopy", Optical Review (submitted).

3. T. Yatsui, S, Sangu, T. Kawazoe, M. Ohtsu, J. Yoo, S. J. An, and **G.-C. Yi**, presentation in The 5th Asia-Pacific Conference on Near-field Optics (2005).

4. T. Yatsui, T. Kawazoe, M. Ohtsu, S. J. An, J. Yoo, and **G.-C. Yi**, proceeding and presentation in IEEE-NANO (2005).

5. T. Yatsui, J. Lim, T. Kawazoe, M. Ohtsu, J. Yoo, S.J. An, and **G.-C. Yi**, presentation in European Materials Research Society meeting (2005).

6. Takashi Yatsui, Jungshik Lim, Tadashi Kawazoe, Motoichi Ohtsu, Sung Jin An, Jinkyoung Yoo, **Gyu-Chul Yi**, proceeding and presentation in CLEO/QELS (2005)